Dalton Transactions

ROYAL SOCIETY OF CHEMISTRY

PAPER

View Article Online
View Journal | View Issue

Cite this: *Dalton Trans.*, 2026, **55**, 4075

Tuning the morphology of ZnCdS@CeO_2 Z-scheme heterostructures from core–shell to core–satellite for superior photocatalytic performance

Yong Liu, Baowei Shen, Sijia Zhao, Guixia Ma, Yujie Ma, Yu Xia, Xing Wang and Yuhua Feng *

In addition to solar cells, photocatalysis is an alternative way for the direct utilization of clean and sustainable solar energy. Currently, the core challenge in photocatalysis is the efficiency of the separation and transfer of the photogenerated electrons (e^-) and holes (h^+) in photocatalysts. Herein, continuous tuning of ZnCdS–CeO_2 heterostructures *via* a seed-mediated growth approach yielded two typical hybrid structures: ZnCdS–CeO_2 core–satellite (ZCSC I) and ZnCdS@CeO_2 core–shell (ZCSC II). Leveraging the Janus configuration of the ZCSC I structure, a marked improvement in charge separation and transfer efficiency was observed in photocurrent and transient fluorescence tests. This enhancement should be due to the electron "sink effect" in the ZCSC I structure, as well as the spatial separation of the ZnCdS (ZCS) and CeO_2 domains. Furthermore, the photocatalytic activity of the heterostructures was evaluated using the photocatalytic degradation of methylene blue (MB) as a model reaction. Consistent with the above tests, the ZCSC I structure showed the highest MB degradation rate of 91% within 60 minutes. From the calculated kinetic rate constants (*k* values), the *k* value of the ZCSC I structure is 4, 2.1, and 1.5 times higher than those of the CeO_2, ZCS, and ZCSC II structures, respectively. Through radical trapping experiments, the ZnCdS–CeO_2 heterostructures were identified as Z-scheme heterojunctions. This work provides solid mechanistic understanding and valuable insights for improving the catalytic efficiency of hybrid photocatalysts, which is helpful for the rational design and precise control of hybrid photocatalysts with high catalytic efficiency and would assist their applications in diverse catalytic reactions.

Received 7th January 2026,
Accepted 2nd February 2026

DOI: 10.1039/d6dt00034g

rsc.li/dalton

1. Introduction

Recently, energy and environmental problems have become the main challenges on a worldwide scale. Extreme interest and effort have been devoted to the development of new clean energy, which may be the ultimate solution to the sustainable development of energy and a clean environment.[1,2] In this context, solar energy has become one of the most suitable energy sources that meets both clean and sustainable requirements.[3–7] Currently, the two primary approaches for solar energy utilization are solar cells and photocatalysis.[8] While solar cells have been successfully commercialized and are undergoing rapid advancement, photocatalysis lags far behind.[9] The main bottleneck is the low quantum efficiency (QE) of solar photocatalysis.[10] In this context, the urgent demand for novel high-QE photocatalyst materials has reached an unprecedented level.

It is widely accepted that the key problem in photocatalysis is the low efficiency of charge separation and transfer of excitons under light irradiation, which stems from the rapid recombination of photogenerated e^- and h^+.[11,12] Various strategies have been developed to address this issue,[13–17] among which the introduction of co-catalysts as e^- or h^+ extractors and the construction of heterojunctions have shown remarkable advantages and great potential for enhancing photocatalytic performance.

Among various combinations of semiconducting materials with different band structures in photocatalytic heterojunctions, enhanced charge separation and migration of carriers (photogenerated e^- and h^+) can only be achieved in type-II heterojunctions with staggered band gaps, which induce the opposite migration of h^+ and e^- across the heterojunction interface. For type-I (straddling gap) and type-III (broken gap) heterostructures, however, the efficiency of charge separation and transportation is low due to the lack of driving force.

Institute of Advanced Synthesis, School of Chemistry and Molecular Engineering, Nanjing Tech University, Nanjing 211816, China. E-mail: ias_yhfeng@njtech.edu.cn

Nevertheless, the enhancements in type-II heterostructures are achieved at the cost of reduced redox capabilities as a result of the transfer of e^- from the higher conduction band (CB) to the lower CB and h^+ from the lower valence band (VB) to the higher VB of the constituent semiconductors, respectively.[18–21] An interesting exception is the Z- or S-scheme photocatalysts, which belong to special type-II heterostructures in terms of band configuration but follow a similar e^- and h^+ transfer pathway to that in the natural photosynthesis process.[22–24] As a result, the high redox capabilities of the constituent materials are retained due to the recombination of h^+ and e^- with relatively low redox potentials at the heterojunction interface. Hence, Z- or S-scheme photocatalysts are highly desired for their prominent dual advantages of enhanced photocatalytic activity and preserved redox potency.[25–30]

In our previous work, in addition to material hybridization, the structural configuration of the constituent materials was found to be essential for realizing the advantages of enhancing photocatalytic efficiency.[31–34] In a core–shell structure, one type of separated charge carrier (e^- or h^+) is forced to migrate to the core and the other to the shell. Ultimately, only the carriers that reach the shell surface can participate in photocatalytic reactions and be consumed. In such a case, the other type of carrier accumulates in the core of the core–shell structure and hinders the subsequent migration of the same type of carrier due to strong repulsive forces. As a result, the efficiency of charge separation decreases progressively until the carriers in the core reach saturation, which completely suppresses charge separation. In contrast to the core–shell structure, the migration of separated e^- and h^+ to different domains in a Janus structure enables both carriers to be consumed in a timely manner upon reaching the surface of spatially separated domains, thus facilitating continuous charge separation and transfer *via* the electron sink effect.[33]

For the construction of Z- or S-scheme photocatalysts, metal sulphides are pivotal components, among which the solid solution of ZnCdS (ZCS) is an ideal candidate based on its narrow band gap (2.35 eV),[35] high charge separation efficiency, excellent chemical stability, and long-term durability.[36–39]

In this work, ZnCdS–CeO_2 heterostructures were synthesized *via* a seed-mediated growth method. ZCS solid solution nanoparticles, which combine the advantages of both ZnS and CdS, were used as seeds for the growth of CeO_2 surface domains. By continuously tuning the growth kinetics of CeO_2 through varying the concentrations of $Ce(AC)_3$, CTAB and K_2PtCl_4, the ZnCdS–CeO_2 heterostructures were fine-tuned from core–shell to core–satellite structures. Systematic investigations revealed that the ZnCdS–CeO_2 heterostructures adopt a Z-scheme configuration, where electron migration follows a Z-shaped pathway mimicking the natural photosynthesis process. Benefiting from enhanced charge separation and migration efficiencies, the ZCSC I structure—with spatially well-separated CeO_2 domains on the surface of ZCS seeds—exhibited superior photocatalytic activity in the model photocatalytic degradation of MB dye compared to that of the ZCSC II structure. Our results demonstrate that, in addition to the formation of the well-established highly efficient Z-scheme electron transfer pathway, the Janus structural configuration is more important for maximizing the photocatalytic activity of hybrid photocatalysts with optimal material combinations.

2. Experimental section

2.1 Chemicals and materials

All chemical reagents were used without further purification. Cadmium acetate dihydrate ($Cd(CH_3COO)_2{\cdot}2H_2O$, 98%) and zinc acetate dihydrate ($Zn(CH_3COO)_2{\cdot}2H_2O$, 98%) were obtained from Sinopharm Chemical Reagent Co., Ltd, China. Thiourea (CH_4N_2S, ≥99%) was purchased from Mallinckrodt. Hexadecyltrimethylammonium bromide (CTAB) was purchased from Sigma-Aldrich (USA). Cerium acetate ($Ce(CH_3CO_2)_3{\cdot}xH_2O$, 99.99%) was purchased from Aladdin. Potassium chloroplatinate (K_2PtCl_4, 98%) and ethanol (EtOH, ≥99.7%) were purchased from China National Pharmaceutical Group Corporation (Sinopharm). All solutions were prepared using ultrapure deionized water (18.3 MΩ).

2.2 Synthesis of ZCS nanospheres

ZCS was synthesized by an improved hydrothermal method.[35] 0.27 g of $Cd(CH_3COO)_2{\cdot}2H_2O$, 0.22 g of $Zn(CH_3COO)_2{\cdot}2H_2O$ and 3.6 g of thiourea were dissolved in 50 mL of deionized (DI) water and stirred for 30 minutes. Then, the solution was transferred to a 100 mL autoclave and stored at 140 °C for 5 hours. After that, the precipitate was centrifuged, washed several times with DI water and ethanol, and finally the product was dispersed in 50 mL of DI water.

2.3 Synthesis of ZCSC I

Typically, 1 mL of the ZCS stock solution was diluted to 10 mL with DI water. A 150 μL aliquot of this diluted ZCS solution was then added to a 5 mL centrifuge tube containing 200 μL of 1 mM CTAB solution. After thorough vortex mixing, 20 μL of 0.1 mM K_2PtCl_4 solution was added. The solution was allowed to stand for 1 min to facilitate the adsorption of $PtCl_4^{2-}$ onto the ZCS surface. Subsequently, 50 μL of freshly prepared 10 mM $Ce(Ac)_3$ solution was added, and the total volume was adjusted to 1 mL with DI water. The resulting mixture was placed in a preheated oven at 100 °C for 1 h to complete the reaction. Finally, the product was collected by centrifugation, rinsed repeatedly, redispersed in DI water, and stored for later use.

2.4 Synthesis of ZCSC II

The preparation of ZCSC I was similar to that of the ZCSC II, except that the CTAB solution was adjusted from 200 μL of 1 mM to 50 μL of 0.1 mM, with the volume of DI water supplemented accordingly to maintain a total reaction volume of 1 mL.

2.5 Characterization

Transmission Electron Microscopy (TEM) images were obtained using an HT7700 TEM (100 kV) and a Talos L120C

model (120 kV). Scanning Electron Microscopy (SEM) images were obtained using a Quanta 250 FEG scanning transmission electron microscope (30 kV). UV-Vis spectra were recorded using a Lambda 750 UV-Vis spectrophotometer. Time-resolved fluorescence spectra (300 nm excitation) were recorded using an Edinburgh FLS980 spectrometer (room temperature). X-ray diffraction (XRD) patterns were obtained using a Rigaku Miniflex-600 advanced powder diffractometer (Cu Kα radiation, λ = 1.5406 Å) in the 2θ range of 10°–80°, with spin-coated samples on quartz substrates. *In situ* X-ray Photoelectron Spectroscopy (XPS) spectra were recorded using a Thermos Fisher ESCALAB 250Xi X-ray photoelectron spectrometer (USA) under dark conditions and after 15 min of xenon lamp irradiation.

3. Results and discussion

The ZCSC I and ZCSC II structures were synthesized *via* a seed-mediated growth method (Fig. 1a). In a typical synthesis, the ZCS seed nanoparticles (with an average diameter of 102 nm, Fig. S1) were synthesized by a hydrothermal method.[35] The ZCS seeds are composed of multiple crystal domains and exhibit a roughly spherical morphology, consistent with the results reported in the literature. The ZnCdS–CeO_2 structures were then synthesized *via* the *in situ* oxidation of $Ce(AC)_3$ using K_2PtCl_4 in the growth solution.[40] After a 1 h reaction, the products were separated by centrifugation at 4000 rpm for 10 min and the concentrated samples were collected by discarding the supernatant for transmission electron microscopy (TEM) characterization (Fig. 1b–d), whereas the as-synthesized sample solution was directly used for absorption spectrum measurements.

As shown in Fig. 2, keeping other conditions the same (CTAB = 200 μM and K_2PtCl_4 = 5 μM, both in the final concentration), a variation in the concentration of the $Ce(AC)_3$ precursor led to the continuous evolution of the ZnCdS–CeO_2 structures from core–satellite to core–shell structures. Specifically, in the absence of $Ce(AC)_3$, no growth of CeO_2 can be observed on the surface of the ZCS seeds (Fig. 2a). At a low $Ce(AC)_3$ concentration of 250 μM, the growth of small CeO_2 islands in a cube shape (with an average diameter of 18.5 nm, Fig. S1) can be observed, giving a typical core–satellite structure (Fig. 2b, denoted as the ZCSC I structure). Fig. S2 presents the size distribution of different composite structures. When the concentration of $Ce(AC)_3$ was increased to 500 μM, the density of the CeO_2 island grown on the surface of the ZCS seeds exhibited a significant increase, (Fig. 2c). Unlike the typical core–satellite structure in Fig. 2b, the dense CeO_2 islands are closely distributed on the surface of the ZCS seeds, forming almost a complete shell that shrouds the ZCS core. As shown in Fig. 2d, when the concentration of $Ce(AC)_3$ was further increased to 1 mM, the growth of a uniform CeO_2 shell on the ZCS seeds can be observed. It should be noted that the CeO_2 shell has an amorphous morphology, different from the small crystal domains in the ZnCdS–CeO_2 structures, as shown in Fig. 2b and c (denoted as the ZCSC II structure). The size distribution of the composite structures regulated by $Ce(AC)_3$ is shown in Fig. S2.

To investigate the influence of the CTAB surfactant, a series of control experiments were conducted (Fig. 3). Under fixed conditions of $Ce(AC)_3$ = 250 μM and K_2PtCl_4 = 5 μM, when the concentration of CTAB was decreased to 50 μM, the ZnCdS–CeO_2 heterostructure changed from the ZCSC I structure to a mixture of the ZCSC I and ZCSCII structures (Fig. 3a). A further decrease in CTAB concentration to 5 μM led to the for-

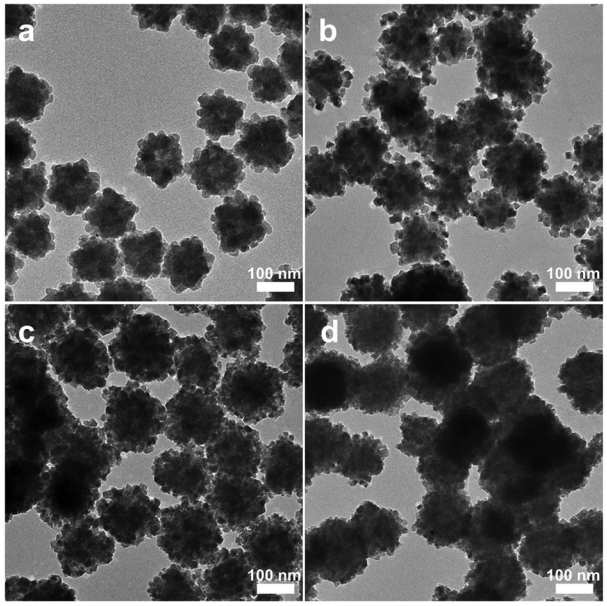

Fig. 2 The representative TEM images of the ZnCdS–CeO_2 hybrid structures at $Ce(AC)_3$ concentrations of (a) 0 μM; (b) 250 μM; (c) 500 μM; and (d) 1 mM.

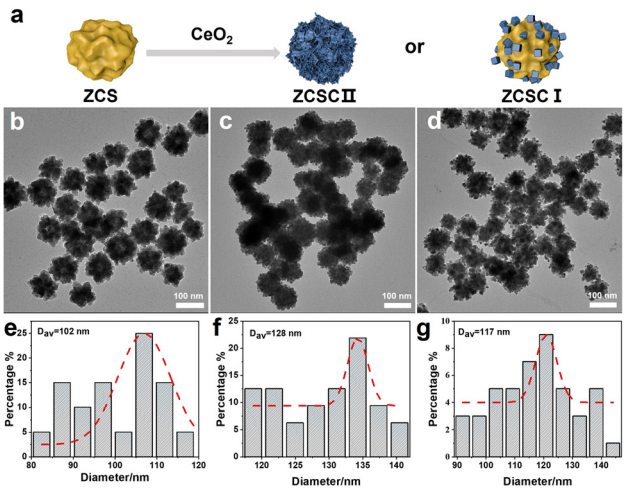

Fig. 1 (a) Schematic illustration of the synthesis of core–shell and core–satellite nanostructures. TEM images of the (b) ZCS, (c) ZCSC II, and (d) ZCSC I structures. Particle size distributions of the (e) ZCS, (f) ZCSC II, and (g) ZCSC I structures.

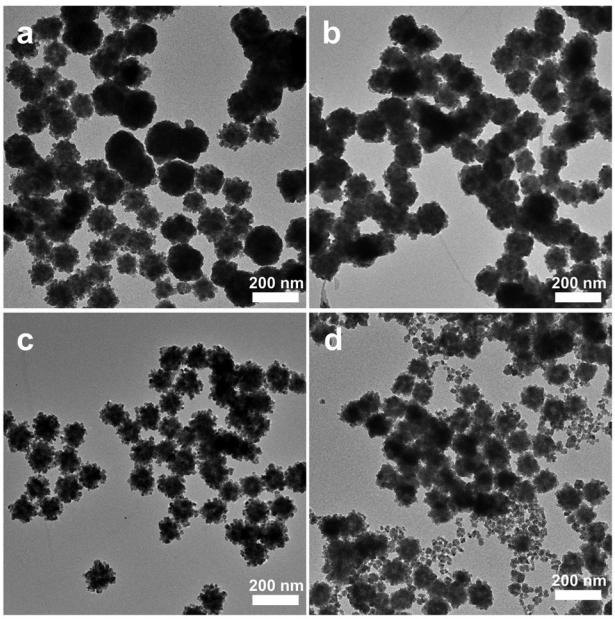

Fig. 3 Effect of the CTAB concentration on the selective growth behaviour. (a–d) Representative TEM images of the products at CTAB concentrations of (a) 50 μM; (b) 5 μM; (c) 1 mM; and (d) 2.5 mM.

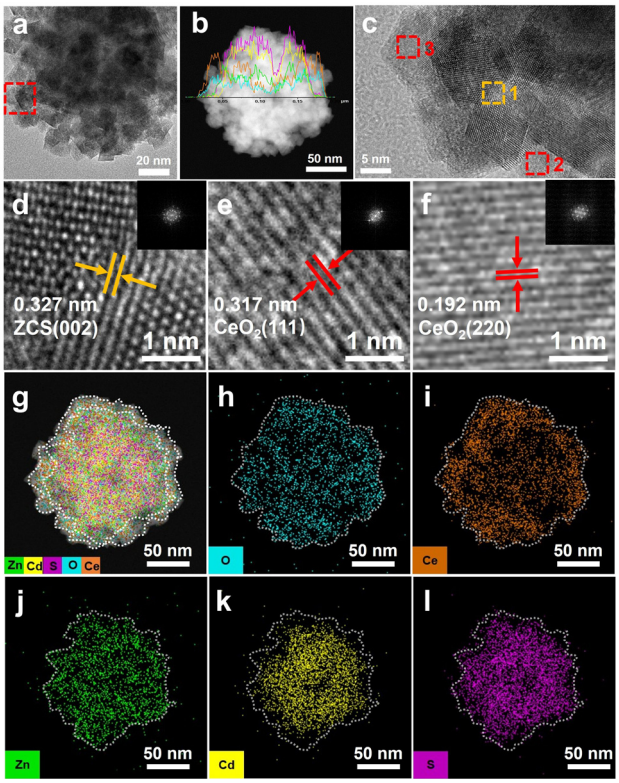

Fig. 4 (a, b, and d–f) HRTEM images; (c) EDS line scan; and (g–l) EDS mapping of an individual ZCSC I structure.

mation of purely the ZCSC II structure (Fig. 3b). This result revealed the effect of CTAB on the growth mode of CeO_2 on ZCS seeds. A lower CTAB concentration facilitated the uniform nucleation and layered growth of CeO_2, possibly due to the decreased interfacial energy between the ZCS and CeO_2 growth materials caused by the reduced surface coverage of CTAB on ZCS. In contrast, a significant increase in the CTAB concentration from 200 to 1 mM did not cause a structural change in the ZCSC I structure (Fig. 3c). When the concentration of CTAB was further increased to 2.5 mM, serious homogeneous nucleation and growth of free CeO_2 nanoparticles were observed (Fig. 3d), indicating the too high interfacial energy between ZCS and CeO_2 due to the increased surface coverage of the ZCS seeds with CTAB. Meanwhile, Table S1 provides the detailed synthetic parameters, and the size distribution of the composite structures regulated by CTAB is shown in Fig. S3. Additionally, the effect of K_2PtCl_4 on the structure is shown in Fig. S4.

To check the detailed crystal structure and composition of the ZnCdS–CeO_2 structure, high-resolution transmission electron microscopy (HRTEM) and energy dispersive X-ray spectroscopy (EDS) characterization studies were carried out on an individual ZCSC I nanoparticle. As shown in Fig. 4a and b, the CeO_2 crystal domain grown on the surface of the ZCS seeds can be more clearly observed in the HRTEM and high-angle annular dark field scanning transmission electron microscopy (HAADF-STEM) images compared to the common TEM images in Fig. 2 and 3. From the HRTEM image in Fig. 4c, the lattice fringes of the ZCS and CeO_2 domains can be obviously observed, indicating the high crystallinity of the ZCSC I structure. In the enlarged HRTEM image of the marked area 1 in Fig. 4d, the 0.327 nm lattice spacing can be ascribed to the *d* spacing between the (002) crystal planes of ZCS.[35] Meanwhile, the lattice spacings of 0.317 nm (Fig. 4e) and 0.192 nm (Fig. 4f) for the marked areas of 2 and 3 in Fig. 4c correspond to the spacings of the (111) and (200) planes of the CeO_2 crystal.[40,41] From the EDS line scan profile (Fig. 4b) and the EDS mapping images (Fig. 4g–l), the presence of the Zn, Cd, S, O and Ce elements can be confirmed, in which the element distribution is consistent with that observed in the HRTEM and HAADF-STEM images. (The EDS spectrum and elemental content of ZCSC I are shown in Fig. S5.) The above results provide direct solid evidence for the successful construction of the ZCSC I-type heterostructure.

To further confirm the phase structure, the ZCSC I structure was then analysed by X-ray powder diffraction (XRD). As shown in Fig. 5a, the diffraction pattern of the ZCSC I structure aligned well with the standard references (ZCS JCPDS #89-2943, CeO_2 JCPDS #34-0394), thus confirming the ZCS and CeO_2 crystal components in the ZCSC I structure.[33,42,43] Specifically, the characteristic ZCS peaks are observed at approximately 26.0°(100), 27.7°(002), 29.5°(101), 38.42°(110), 50.2°(103), and 54.5°(112), while the CeO_2 peaks appear at 28.5°(111), 33.1°(200), 47.5°(220), and 56.3°(311). In addition, the sharp diffraction peaks and the absence of significant peak broadening indicate high crystallinity. Thus, XRD analysis verifies the presence of ZCS and CeO_2, as well as the well-defined crystal structure and distinct phase distribution of

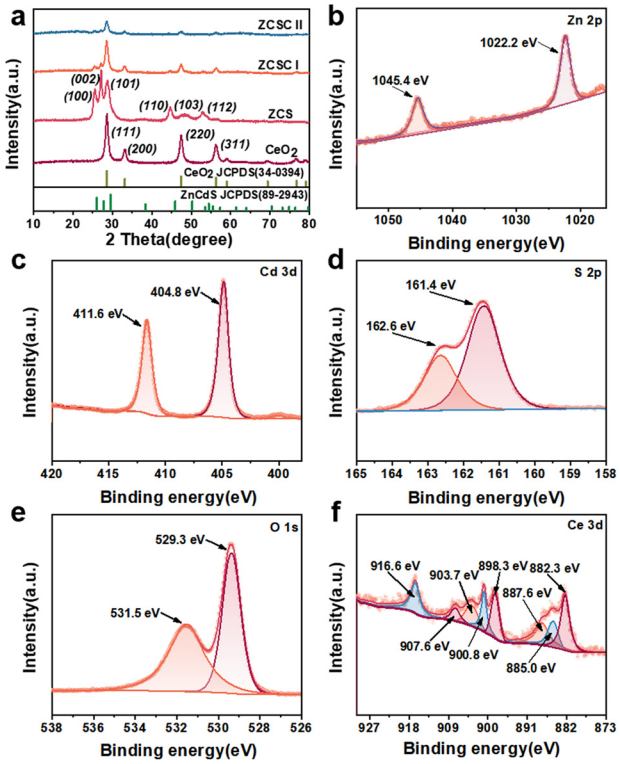

Fig. 5 (a) XRD patterns and (b–f) XPS spectra of the ZCSC I nanoparticles.

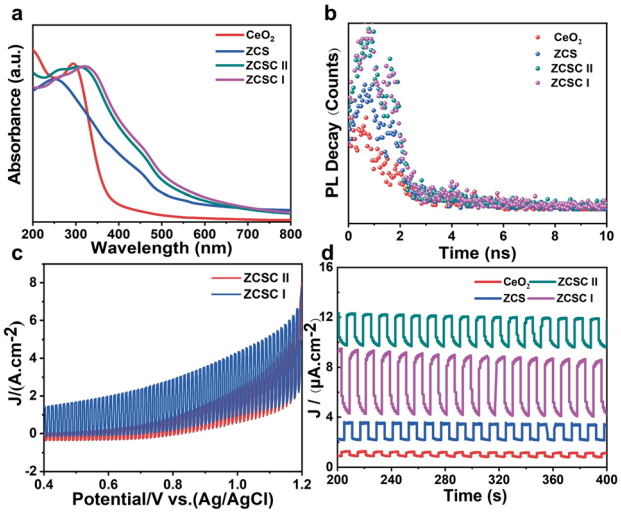

Fig. 6 (a) Absorption spectra; (b) TF spectra of the CeO_2, ZCS, ZCSC I, and ZCSC II structures; (c) linear sweep voltammetry; and (d) *I*–*t* curves.

these materials. The valence state of the elements in ZCSC I was also analysed by X-ray photoelectron spectroscopy (XPS). In Fig. 5b, the high-resolution Zn 2p XPS spectrum of ZCSC I is split into two peaks at 1022.2 and 1045.4 eV, which can be indexed to Zn $2p_{3/2}$ and Zn $2p_{1/2}$, respectively. The peaks of Cd 3d in Fig. 5c at 404.8 and 411.6 eV can be assigned to Cd $3d_{5/2}$ and Cd $3d_{3/2}$. The peaks at 161.4 and 162.6 eV correspond to S $2p_{3/2}$ and $2p_{1/2}$ (Fig. 5d).[35,44] In the O 1s spectrum, the peak at 529.3 eV is assigned to the crystal lattice oxygen (Ce(IV)–O bond), while the peak at 531.5 eV can be assigned to the O in O–H bond from the water chemisorbed on the surface of the CeO_2 island (Fig. 5e). In Fig. 5f, the Ce 3d spectrum exhibits main and satellite peaks at 882.3, 887.6, and 898.3 eV (Ce $3d_{3/2}$) and at 900.8, 907.6, and 916.6 eV (Ce $3d_{5/2}$), corresponding to Ce^{4+}.[33] The high-resolution spectrum of the C 1s orbital and the full elemental spectrum are shown in Fig. S6. These results confirmed the valence state of the composed elements, which are consistent with the designed ZCSC I heterostructure.

As can be seen in the absorption spectra in Fig. 6a, the characteristic absorption peak of CeO_2 is close to 294 nm. The characteristic absorption peak of ZCS appears at around 251 nm. Characteristic absorption peaks are observed for ZCSC I at 310 nm and for ZCSC II at 325 nm. Compared with CeO_2 and ZCS, ZCSC I and ZCSC II exhibited stronger light absorption in the visible light region owing to the synergistic absorption of ZCS and CeO_2. Notably, when CeO_2 was supported on ZCS nanospheres, the band-edge positions of ZCSC I and ZCSC II exhibit a red shift. The enhanced absorption in the visible light region is conducive to boosting the photocatalytic activity. As shown in Fig. 6b, ZCSC I showed the longest fluorescence lifetime in the transient fluorescence (TF) spectra, followed by ZCSC II, ZCS, and CeO_2. The calculated lifetime of carriers followed the same sequence, which are 4.56 ns for ZCSC I, 4.21 ns for ZCSC II, 1.10 ns for ZCS and 1.05 ns for CeO_2, respectively (Table S2 and Fig. S7). These results confirmed that the formation of a heterostructure led to an obvious prolonged lifetime of the carrier, *i.e.*, the higher separation efficiency of the photogenerated electrons and holes. To evaluate the charge separation efficiency, Linear Sweep Voltammetry (LSV) and photocurrent generation tests were performed on the composite catalyst. As shown in Fig. 6c, with an increase in potential, the current densities of both ZCSC I and ZCSC II exhibit a gradual increase; however, the current density of ZCSC I is markedly higher than that of ZCSC II, demonstrating that the charge separation efficiency of ZCSC I is far superior to that of ZCSC II. Meanwhile, the photocurrent response of ZCSC I and ZCSC II clearly shows that their electron–hole separation rate is much larger than those of CeO_2 and ZCS, as shown in Fig. 6d. The photocurrent density of ZCSC I reaches 5.11 μA cm^{-2}, which is 14.6, 4.05 and 2.08 times that of pristine CeO_2 (0.35 μA cm^{-2}), pristine ZCS (1.26 μA cm^{-2}) and ZCSC II (2.46 μA cm^{-2}), respectively. Based on the similar charge transfer resistance observed in electrochemical impedance spectroscopy (EIS, Fig. S8), the core–satellite structure showed obvious superiority in charge separation efficiency compared to the core–shell counterpart. The reduced performance of ZCSC II is primarily ascribed to the CeO_2 fully covering the ZCS surface, which impedes electron transport to the surface and thus promotes electron–hole recombination.

Based on the absorption spectra and the transformed data using the Tauc function, the direct band gaps (E_g) of the ZCS

and CeO_2 semiconductors can be estimated to be 2.02 and 3.30 eV, respectively (Fig. 7a and b).[45,46] Based on the positive slopes of the Mott–Schottky (M–S) curves (Fig. 7c and d), both ZCS and CeO_2 are n-type semiconductors.[47] The conduction band (CB) edges of ZCS and CeO_2 were calculated from the M–S plots to be −0.84 and −0.35 eV, respectively (*vs.* Ag/AgCl, pH = 7), corresponding to −0.643 and −0.153 eV *vs.* NHE at pH = 7. Based on the above data of the bandgap and the CB, the valence band (VB) edges of ZCS and CeO_2 were calculated as 1.377 and 3.147 eV (*vs.* NHE, pH = 7), respectively. The higher VB and CB positions of ZCS compared to those of CeO_2 indicate the possible type II or Z-scheme electron transfer pathway in the heterostructure.

To evaluate the photocatalytic activity of the ZnCdS–CeO_2 catalysts, photocatalytic degradation of MB was systematically investigated by using pure ZCS, CeO_2, ZCSC I and ZCSC II as reference samples. As shown in Fig. 8a, the adsorption–desorption equilibrium of MB in the catalysts can be reached in 60 min within the dark. Then, after irradiation under a Xe lamp for 60 min, the ZCSC I structure showed the highest degradation efficiency of 91.0%, followed by ZCSC II (81.3%), ZCS (71.0%) and CeO_2 (45.1%). Fig. 8b depicts the changes in the absorbance intensity of MB under Xe lamp irradiation at 10 min time intervals using ZCSC I as the catalyst. With prolonged light irradiation, the intensity of the absorption peak of MB at 664 nm showed a continuous decrease. As shown in the inset of Fig. 8b, the blue colour of the MB solution also showed a gradual decrease and became almost colourless after 40 min. To investigate the active species involved in the photocatalytic degradation of MB using ZCSC I as the catalyst, silver nitrate ($AgNO_3$), ethylenediaminetetraacetic acid disodium salt (EDTA-2Na), benzoquinone (BQ) and isopropanol (IPA) scavengers were used to capture the photogenerated e^-/h^+, superoxide radicals ($^{\bullet}O^{2-}$) and hydroxyl radicals ($^{\bullet}OH$).[48,49] As shown in Fig. 8c and d, the addition of BQ and $AgNO_3$ led to a decrease in the MB degradation efficiency to approximately 22% and 48% of that without scavengers, revealing that $^{\bullet}O^{2-}$ and e^- are the dominant active species for the photocatalytic degradation of MB. Meanwhile the slight inhibition of MB degradation in the presence of IPA and EDTA-2Na suggested the minor contribution of the photogenerated $^{\bullet}OH$ and h^+ to the degradation of MB. In addition, from the electron paramagnetic resonance (EPR) characterization studies (Fig. 8e and f), no free radicals were detected under dark conditions. In contrast, distinct characteristic peaks of DMPO-$^{\bullet}O^{2-}$ and DMPO-$^{\bullet}OH$ were observed under light irradiation, indicating the presence of $^{\bullet}O^{2-}$ and $^{\bullet}OH$ in the photocatalytic degradation process. The above results confirmed the generation of $^{\bullet}OH$ radicals during the photocatalytic degradation of MB using ZCSC I as the catalyst. To evaluate the durability of ZCSC I, cyclic photocatalytic experiments were conducted over four consecutive cycles. As shown in Fig. S9, the photodegradation efficiency of MB dye under visible-light irradiation was recorded for each cycle, and only a slight decrease in efficiency was observed after four cycles of testing. Kinetic rate constants (k values) were obtained by plotting $\ln(C/C_0)$ against the time, and a strong linear relationship was found between $\ln(C/C_0)$ and the time, as shown in Fig. S10.

Based on the above results, under light irradiation, the electron migration pathway in the ZCSC I catalyst should follow a

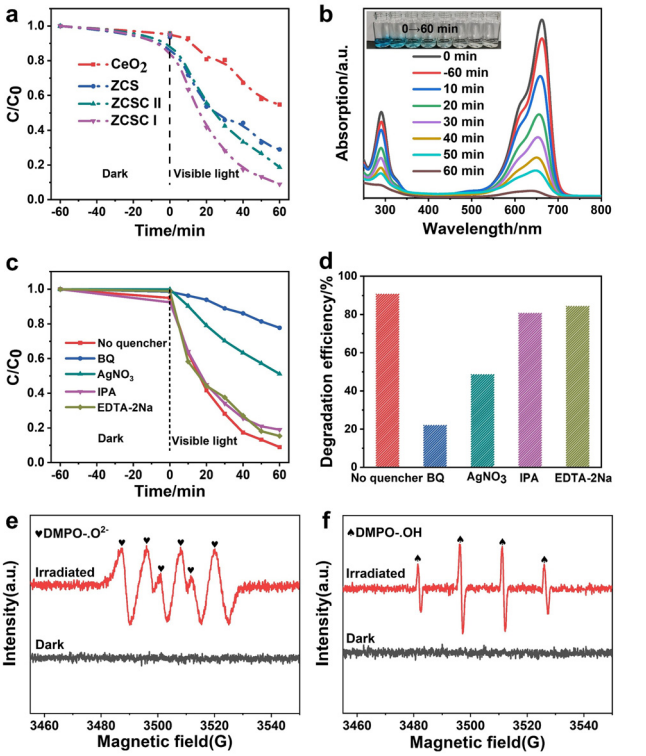

Fig. 8 (a) MB photodegradation efficiency *vs.* time curves with different nanostructures (control catalysts); (b) UV-Vis spectra of MB degraded by ZCSC I; (c and d) MB photodegradation efficiency *vs.* time curves with different scavengers; and (e and f) EPR spectra of DMPO-$^{\bullet}O^{2-}$ and DMPO-$^{\bullet}OH$.

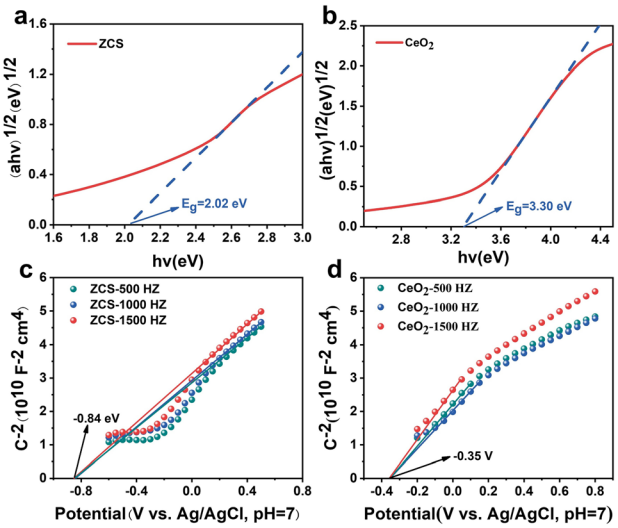

Fig. 7 (a and b) Tauc plots of ZCS and CeO_2 and (c and d) Mott–Schottky plots of ZCS and CeO_2.

Z-scheme pathway. Specifically, the higher (lower) work function (Fermi level) of CeO_2 would lead to the migration of e^- from ZCS to CeO_2 until the establishment of an equal Fermi level at the interface,[50] which causes band bending and the formation of an internal electric field directed from ZCS to CeO_2 across the interface. The rectifying effect of the internal electric field can regulate the electron flow and inhibit the recombination of h^+ and e-.[51,52] Under light irradiation, the excited e^- in the VB of ZCS and CeO_2 move to the CB, leaving h^+ in their respective VB. In conventional type-II heterojunctions, the e^- in the CB of ZCS would move to the CB of CeO_2, while the h^+ in the VB of CeO_2 migrate to the VB of ZCS. In a type-II heterojunction, the separation of the photogenerated h^+ and e^- can be promoted, but this comes at the cost of reduced redox ability; consequently, $^{\bullet}O^{2-}$ and $^{\bullet}OH$ cannot be generated. From the active species capture experiments in Fig. 8, the presence and the important role of $^{\bullet}O^{2-}$ and $^{\bullet}OH$ in the photocatalytic degradation of MB were confirmed. Therefore, in the ZCSC I heterostructure, the photogenerated e^- in the CB of CeO_2 should migrate to the VB of ZCS and recombine with h^+ therein. As a result, h^+ would be left at the VB of CeO_2 and e^- at the CB of ZCS, forming a Z-scheme electron transportation pathway (Fig. 9). Since the EVB (CeO_2) > $E(OH^-/^{\bullet}OH)$, $^{\bullet}OH$ can be generated at the VB of CeO_2. Meanwhile, as the ECB (ZCS) < $E(O_2/^{\bullet}O^{2-})$, $^{\bullet}O^{2-}$ can be generated at the CB of ZCS. As a result of the Z-scheme electron transportation mechanism, in addition to the enhanced charge separation efficiency, the photogenerated e^- and h^+ and the produced $^{\bullet}O^{2-}$ and $^{\bullet}OH$ retain higher redox ability, making the catalyst suitable for a broader range of catalytic reactions. Eqn (1)–(6) in Fig. 9b illustrate the possible mechanism for the photocatalytic degradation of MB using ZnCdS–CeO_2.[53–56]

It should be noted that under the same mechanism, the generation of $^{\bullet}O_2^-$ in the core–shell ZCSC II structure needs a one more step, in which the photogenerated e^- at the core ZCS domain must transfer to the shell surface to react with O_2 in the solution to generate $^{\bullet}O_2^-$ (Fig. S11). During their transfer across the CeO_2 shell, the recombination with photogenerated holes would significantly cause a decrease in the efficiency of the generation of both $^{\bullet}O_2^-$ and $^{\bullet}OH$ species. Hence, the core–satellite ZCSC I structure is an ideal photocatalyst with highly efficient catalytic activity than the core–shell ZCSC II structure.

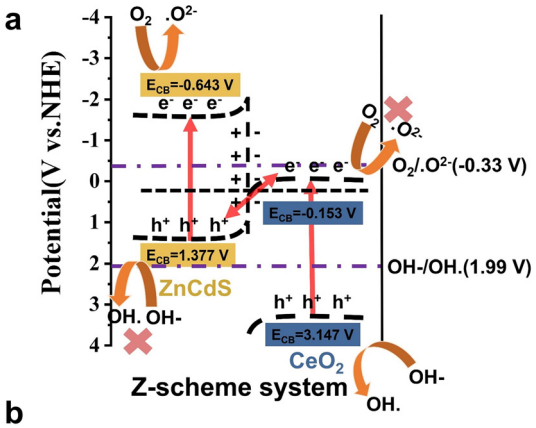

b

$$ZnCdS\text{-}CeO_2 + h\nu \rightarrow e^-(ZnCdS) + h^+(CeO_2) \quad (1)$$

$$e^- + O_2 \rightarrow {}^{\bullet}O^{2-} \quad (2)$$

$$h^+ + OH^- \rightarrow {}^{\bullet}OH \quad (3)$$

$${}^{\bullet}O^{2-} + MB \rightarrow H_2O + CO_2 \quad (4)$$

$${}^{\bullet}OH + MB \rightarrow H_2O + CO_2 \quad (5)$$

$$h^+ + MB \rightarrow H_2O + CO_2 \quad (6)$$

Fig. 9 (a) Schematic diagram of the Z-scheme charge transfer pathway in the ZCSC I heterostructure under light irradiation. (b) The reaction pathways (1)–(6) for the degradation of MB over the ZnCdS–CeO_2 photocatalyst.

4. Conclusion

In summary, the continuous tuning of a ZnCdS–CeO_2 hybrid semiconductor photocatalyst from core–shell to core–satellite structures *via* a seeded growth process was successfully achieved. With decreasing coverage of the CeO_2 crystalline islands on the surface of ZCS, the ZCS and CeO_2 domains gradually separated, forming a Janus configuration. From the photocurrent generation and TF measurements, the charge separation efficiency increased with the decrease in the density of the surface of CeO_2 islands. The main reason is the exciton sink effect, in which the photogenerated e^- and h^+ were driven by the internal electric field at the interface to migrate to the physically separated domains on the exposed surfaces of ZCS and CeO_2, and thus can be immediately utilized. As a result, the ZCSC I structure showed superior catalytic activity in the model reaction of MB photocatalytic degradation compared with the ZCSC II structure. In the active species capture experiment during the photocatalytic degradation of MB, the ZnCdS–CeO_2 hybrid semiconductor was confirmed to be a Z-scheme type heterojunction, which possesses stronger redox ability than the type-II heterojunction with the same structure and constituent materials. In this work, the precise structure control and the Janus configuration of the ZCS and CeO_2 domains in the ZCSC II structure were confirmed to be the key factors for promoting the efficiency of the photocatalytic reaction. Our results provide a helpful reference for the rational design and synthesis of highly efficient photocatalysts in the Janus structure suitable for catalysing various reactions. Further improvements such as the eradication of possible Cd^{2+} leaching during long-term catalysis and the optimization of scalable synthesis may eventually assist their wide practical applications.

Author contributions

Yong Liu: investigation, data curation, and writing – review and editing. Baowei Shen: investigation and data curation. Sijia Zhao, Guixia Ma, Yujie Ma, Yu Xia, and Xing Wang:

writing – review and editing. Yuhua Feng: conceptualization, methodology, writing – review & editing, and supervision. All authors contributed to the general discussion.

Conflicts of interest

The authors declare no conflicts of interest.

Data availability

Data supporting the conclusions of this manuscript can be found in the supplementary information (SI). Supplementary information is available. See DOI: https://doi.org/10.1039/d6dt00034g.

Acknowledgements

This work was financially supported by the start-up fund at Nanjing Tech University (39837140) and The Jiangsu Science and Technology Plan (BK20211258).

References

1 I. Ahmad, Y. Zou, J. Yan, Y. Liu, S. Shukrullah, M. Y. Naz, H. Hussain, W. Q. Khan and N. R. Khalid, Semiconductor photocatalysts: A critical review highlighting the various strategies to boost the photocatalytic performances for diverse applications, *Adv. Colloid Interface Sci.*, 2023, **311**, 102830.
2 Z. Wang, Z. Lin, S. Shen, W. Zhong and S. Cao, Advances in designing heterojunction photocatalytic materials, *Chin. J. Catal.*, 2021, **42**, 710–730.
3 H. Song, S. Luo, H. Huang, B. Deng and J. Ye, Solar-Driven Hydrogen Production: Recent Advances, Challenges, and Future Perspectives, *ACS Energy Lett.*, 2022, **7**, 1043–1065.
4 X. Sun, S. Jiang, H. Huang, H. Li, B. Jia and T. Ma, Solar Energy Catalysis, *Angew. Chem., Int. Ed.*, 2022, **61**, e202204880.
5 B. Fang, Z. Xing, D. Sun, Z. Li and W. Zhou, Hollow semiconductor photocatalysts for solar energy conversion, *Adv. Powder Mater.*, 2022, **1**, 10021.
6 K. Li, B. Peng and T. Peng, Recent Advances in Heterogeneous Photocatalytic CO_2 Conversion to Solar Fuels, *ACS Catal.*, 2016, **6**, 7485–7527.
7 Q. Li, Y. Ouyang, H. Li, L. Wang and J. Zeng, Photocatalytic Conversion of Methane: Recent Advancements and Prospects, *Angew. Chem., Int. Ed.*, 2021, **61**, e202108069.
8 B. Wang, G. M. Biesold, M. Zhang and Z. Lin, Amorphous inorganic semiconductors for the development of solar cell, photoelectrocatalytic and photocatalytic applications, *Chem. Soc. Rev.*, 2021, **50**, 6914–6949.
9 M. Gao, T. Zhang and G. W. Ho, Advances of photothermal chemistry in photocatalysis, thermocatalysis, and synergetic photothermocatalysis for solar-to-fuel generation, *Nano Res.*, 2022, **15**, 9985–10005.
10 O. Henrotte, S. Saris, F. Gröbmeyer, C. G. Gruber, I. Bilgin, A. Högele, N. J. Halas, P. Nordlander, E. Cortés and A. Naldoni, Spatially resolved photocatalytic active sites and quantum efficiency in a 2D semiconductor, *Nat. Commun.*, 2025, **16**, 6904.
11 S. Wu and X. Quan, Design Principles and Strategies of Photocatalytic H_2O_2 Production from O_2 Reduction, *ACS ES&T Eng.*, 2022, **2**, 1068–1079.
12 H. Guo, S. Wang, X. Chen, J. Kou, G. He, Z. Dong and Y. Yan, Engineering a covalent organic framework-based type-II heterojunction for enhanced photocatalytic H_2O_2 synthesis, *Nat. Synth.*, 2025, **4**, 1610–1620.
13 X. Li, Y. Chen, Y. Tao, L. Shen, Z. Xu, Z. Bian and H. Li, Challenges of photocatalysis and their coping strategies, *Chem Catal.*, 2022, **2**, 1315–1345.
14 S. B. Beil, S. Bonnet, C. Casadevall, R. J. Detz, F. Eisenreich, S. D. Glover, C. Kerzig, L. Næsborg, S. Pullen, G. Storch, N. Wei and C. Zeymer, Challenges and Future Perspectives in Photocatalysis: Conclusions from an Interdisciplinary Workshop, *JACS Au*, 2024, **4**, 2746–2766.
15 S. A. Abey, N. M. Reis, E. A. C. Emanuelsson and A. J. Expósito, Harnessing visible light: Advanced photocatalytic strategies for sustainable environmental reactions, *Chem. Eng. J.*, 2025, **519**, 164951.
16 N. Sun, X. Si, L. He, J. Zhang and Y. Sun, Strategies for enhancing the photocatalytic activity of semiconductors, *Int. J. Hydrogen Energy*, 2024, **58**, 1249–1265.
17 H. Wang, X. Li, X. Zhao, C. Li, X. Song, P. Zhang, P. Huo and X. Li, A review on heterogeneous photocatalysis for environmental remediation: From semiconductors to modification strategies, *Chin. J. Catal.*, 2022, **43**, 178–214.
18 A. Balapure, J. R. Dutta and R. Ganesan, Recent advances in semiconductor heterojunctions: a detailed review of the fundamentals of photocatalysis, charge transfer mechanism and materials, *RSC Appl. Interfaces*, 2024, **1**, 43–69.
19 J. Low, J. Yu, M. Jaroniec, S. Wageh and A. A. Al-Ghamdi, Heterojunction Photocatalysts, *Adv. Mater.*, 2017, **29**, 1601694.
20 H. Li, W. Tu, Y. Zhou and Z. Zou, Z-Scheme Photocatalytic Systems for Promoting Photocatalytic Performance: Recent Progress and Future Challenges, *Adv. Sci.*, 2016, **3**, 1500389.
21 Q. Xu, L. Zhang, B. Cheng, J. Fan and J. Yu, S-Scheme Heterojunction Photocatalyst, *Chem*, 2020, **6**, 1543–1559.
22 L. Sun, Z. Zhang, J. Bian, F. Bai, H. Su, Z. Li, J. Xie, R. Xu, J. Sun, L. Bai, C. Chen, Y. Han, J. Tang and L. Jing, A Z-Scheme Heterojunctional Photocatalyst Engineered with Spatially Separated Dual Redox Sites for Selective CO_2 Reduction with Water: Insight by In Situ micros-Transient Absorption Spectra, *Adv. Mater.*, 2023, **35**, e2300064.
23 Y. Zhong, M. Li, X. Luan, F. Gao, H. Wu, J. Zi and Z. Lian, Ultrathin $ZnIn_2S_4$/ZnSe heteronanosheets with modulated S-scheme enable high efficiency of visible-light-responsive

photocatalytic hydrogen evolution, *Appl. Catal., B*, 2023, **335**, 122859.
24 L. Wang, J. Sun, B. Cheng, R. He and J. Yu, S-Scheme Heterojunction Photocatalysts for H_2O_2 Production, *J. Phys. Chem. Lett.*, 2023, **14**, 4803–4814.
25 Q. Xu, L. Zhang, J. Yu, S. Wageh, A. A. Al-Ghamdi and M. Jaroniec, Direct Z-scheme photocatalysts: Principles, synthesis, and applications, *Mater. Today*, 2018, **21**, 1042–1063.
26 N. Ma, C. Lu, Y. Liu, T. Han, W. Dong, D. Wu and X. Xu, Direct Z-Scheme Heterostructure of Vertically Oriented SnS_2 Nanosheet on $BiVO_4$ Nanoflower for Self-Powered Photodetectors and Water Splitting, *Small*, 2024, **20**, e2304839.
27 X. Yu, J. Xu, J. Wang, J. Qiu, X. An, Z. Wang, G. Lv, L. Liao and J. Ye, Mimicking Photosynthesis: A Natural Z-Scheme Photocatalyst Constructed from Red Mud Bauxite Waste for Overall Water Splitting, *Angew. Chem., Int. Ed.*, 2023, **62**, e202302050.
28 X. He, J. Wu, K. Li, M. Liu, H. Shi, J. Du, C. Song, X. Wang and X. Guo, Z-Scheme 2D/2D heterojunction of $ZnIn_2S_4$/Ti-BPDC enhancing photocatalytic hydrogen evolution under visible light irradiation, *Sci. China Mater.*, 2023, **66**, 3155–3164.
29 F.-Z. Chen, Y.-J. Li, M. Zhou, X.-X. Gong, Y. Gao, G. Cheng, S.-B. Ren and D.-M. Han, Smart multifunctional direct Z-scheme In_2S_3@PCN-224 heterojunction for simultaneous detection and photodegradation towards antibiotic pollutants, *Appl. Catal., B*, 2023, **328**, 122517.
30 Y. Deng, Y. Wang, Z. Di, M. Xie, F. Dai, S. Zhan and Z. Zhang, Confining Metal-Organic Framework in the Pore of Covalent Organic Framework: A Microscale Z-Scheme System for Boosting Photocatalytic Performance, *Small Methods*, 2022, **6**, e2200265.
31 W. Xu, J. Jia, T. Wang, C. Li, B. He, J. Zong, Y. Wang, H. J. Fan, H. Xu, Y. Feng and H. Chen, Continuous Tuning of Au-Cu_2O Janus Nanostructures for Efficient Charge Separation, *Angew. Chem., Int. Ed.*, 2020, **59**, 22246–22251.
32 R. Xiao, J. Zhang, T. Jiang, Y. Zhou, Y. Wang, W. Xu and Y. Feng, Highly ordered Janus CdS-Au-TiO_2 Z-scheme structure with high efficiency in photocatalysis, *Sci. China: Chem.*, 2023, **66**, 1722–1730.
33 B. Shen, Y. Xia, Y. Zhou, J. Wang, Y. Feng and W. Xu, Synthesis of highly-ordered ternary CeO_2-AuNR-Cu_2O Janus structure with dual Schottky junctions for highly efficient photocatalysis, *Sci. China: Chem.*, 2025, **68**, 1906–1917.
34 Y. Wang, J. Jia, J. Zhang, R. Xiao, W. Xu and Y. Feng, Modulating the Charge Transfer Plasmon in Bridged Au Core-Satellite Homometallic Nanostructures, *Small*, 2023, **19**, e2207907.
35 H. Li, S. Tao, S. Wan, G. Qiu, Q. Long, J. Yu and S. Cao, S-scheme heterojunction of ZnCdS nanospheres and dibenzothiophene modified graphite carbon nitride for enhanced H_2 production, *Chin. J. Catal.*, 2023, **46**, 167–176.
36 S. M. Ghoreishian, K. S. Ranjith, B. Park, S.-K. Hwang, R. Hosseini, R. Behjatmanesh-Ardakani, S. M. Pourmortazavi, H. U. Lee, B. Son, S. Mirsadeghi, Y.-K. Han and Y. S. Huh, Full-spectrum-responsive Bi_2S_3@CdS S-scheme heterostructure with intimated ultrathin RGO toward photocatalytic Cr(VI) reduction and H_2O_2 production: Experimental and DFT studies, *Chem. Eng. J.*, 2021, **419**, 129530.
37 S. M. Ghoreishian, G. S. R. Raju, E. Pavitra, C. H. Kwak, Y.-K. Han and Y. S. Huh, Ultrasound-assisted heterogeneous degradation of tetracycline over flower-like rGO/$CdWO_4$ hierarchical structures as robust solar-light-responsive photocatalysts: Optimization, kinetics, and mechanism, *Appl. Surf. Sci.*, 2019, **489**, 110–122.
38 S. Mirsadeghi, S. M. Ghoreishian, H. Zandavar, R. Behjatmanesh-Ardakani, E. Naghian, M. Ghoreishian, A. Mehrani, N. Abdolhoseinpoor, M. R. Ganjali, Y. S. Huh and S. M. Pourmortazavi, In-depth insight into the photocatalytic and electrocatalytic mechanisms of $Mg_3V_2O_8$@$Zn_3V_2O_8$@ZnO ternary heterostructure toward linezolid: Experimental and DFT studies, *J. Environ. Chem. Eng.*, 2023, **11**, 109106.
39 A. Sheik, K. S. Ranjith, S. M. Ghoreishian, Y. Yang, Y. Park, S. Son, Y.-K. Han and Y. S. Huh, Green approach for the fabrication of dual-functional S/N doped graphene tagged ZnO nanograins for in vitro bioimaging and water pollutant remediation, *Environ. Pollut.*, 2024, **343**, 123077.
40 H. Jia, A. Du, H. Zhang, J. Yang, R. Jiang, J. Wang and C. Y. Zhang, Site-Selective Growth of Crystalline Ceria with Oxygen Vacancies on Gold Nanocrystals for Near-Infrared Nitrogen Photofixation, *J. Am. Chem. Soc.*, 2019, **141**, 5083–5086.
41 H. Jia, M. Zhao, A. Du, Y. Dou and C. Y. Zhang, Symmetry-breaking synthesis of Janus Au/CeO_2 nanostructures for visible-light nitrogen photofixation, *Chem. Sci.*, 2022, **13**, 13060–13067.
42 D. Qin, Y. Xia, Q. Li, C. Yang, Y. Qin and K. Lv, One-pot calcination synthesis of $Cd_{0.5}Zn_{0.5}S$/g-C_3N_4 photocatalyst with a step-scheme heterojunction structure, *J. Mater. Sci. Technol.*, 2020, **56**, 206–215.
43 S. Zhao, J. Huang, Q. Huo, X. Zhou and W. Tu, A non-noble metal MoS_2–$Cd_{0.5}Zn_{0.5}S$ photocatalyst with efficient activity for high H_2 evolution under visible light irradiation, *J. Mater. Chem. A*, 2016, **4**, 193–199.
44 L. Meng, Q. Chen, X. Li, H. Zhang, Y. Hai, Y. Yang, X. Wang and M. Luo, Enhanced Photocatalytic Nitrogen Reduction via Bismuth Nanoparticle-Decorating ZnCdS Solid Solution, *Inorg. Chem.*, 2024, **63**, 5065–5075.
45 P. Guo, X. Liu, P. Zhang, D. Zhang, W. Liu, H. Gao, M. Zhang, H. Xie, R. Wang, Z. Zhang and S. Qiu, Popcorn-like ZnCdS-based nanospheres with hierarchical tandem heterojunctions synergy for efficient photocatalytic performance, *Sep. Purif. Technol.*, 2023, **323**, 124482.
46 R. Jiang, L. Mao, Y. Zhao, J. Zhang, E. B. Chubenko, V. Bondarenko, Y. Sui, X. Gu and X. Cai, 1D/2D CeO_2/$ZnIn_2S_4$ Z-scheme heterojunction photocatalysts for efficient H_2 evolution under visible light, *Sci. China Mater.*, 2022, **66**, 139–149.
47 M. Zhang, X. Zhao, Y. Dong, C. Hu, X. Xiang, X. Zeng, J. Jia, C. Jin, L. Ding and X. Chen, *In situ* synthesis of 0D/1D CeO_2/$Zn_{0.4}Cd_{0.6}S$ S-scheme heterostructures for boosting

photocatalytic remove of antibiotic and chromium, *Ceram. Int.*, 2023, **49**, 5842–5853.

48 A. Trenczek-Zajac, M. Synowiec, K. Zakrzewska, K. Zazakowny, K. Kowalski, A. Dziedzic and M. Radecka, Scavenger-Supported Photocatalytic Evidence of an Extended Type I Electronic Structure of the TiO_2@Fe_2O_3 Interface, *ACS Appl. Mater. Interfaces*, 2022, **14**, 38255–38269.

49 K. Li, C. Tang, R. Xiong, Y. Xiao, B. Cheng and S. Lei, Vacancy-Mediated Z-Scheme Heterostructure in SnO_2-Decorated Spinel $In_{3-x}S_4$ with Boosted Photocatalytic Activity, *Inorg. Chem.*, 2023, **62**, 543–556.

50 X. Cai, J. Du, G. Zhong, Y. Zhang, L. Mao and Z. Lou, Constructing a $CeO_2/Zn_xCd_{1-x}In_2S_4$ S-Scheme Hollow Heterostructure for Efficient Photocatalytic H_2 Evolution, *Acta Phys.-Chim. Sin.*, 2023, **39**, 2302017.

51 Y. Yao, G. Wu, F. Lu, S. Wang, Y. Hu, J. Zhang, W. Huang and F. Wei, Enhanced photo-Fenton-like process over Z-scheme $CoFe_2O_4$/g-C_3N_4 Heterostructures under natural indoor light, *Environ. Sci. Pollut. Res.*, 2016, **23**, 21833–21845.

52 C.-Y. Pei, T. Li, M. Zhang, J.-W. Wang, L. Chang, X. Xiong, W. Chen, G.-B. Huang and D.-M. Han, Synergistic effects of interface coupling and defect sites in $WO_3/InVO_4$ architectures for highly efficient nitrogen photofixation, *Sep. Purif. Technol.*, 2022, **290**, 120875.

53 K. S. Ranjith, D. R. Kumar, S. M. Ghoreishian, Y. S. Huh, Y.-K. Han and R. T. R. Kumar, A radially controlled ZnS interlayer on ultra-long ZnO–Gd_2S_3 core–shell nanorod arrays for promoting the visible photocatalytic degradation of antibiotics, *Nanoscale*, 2020, **12**, 14047–14060.

54 S. M. Ghoreishian, G. S. R. Raju, E. Pavitra, C. H. Kwak, Y.-K. Han and Y. S. Huh, Controlled synthesis of hierarchical α-nickel molybdate with enhanced solar-light-responsive photocatalytic activity: A comprehensive study on the kinetics and effect of operational factors, *Ceram. Int.*, 2019, **45**, 12041–12052.

55 E. Pavitra, G. S. R. Raju, S. M. Ghoreishian, C. H. Kwak, J. Y. Park, Y.-K. Han and Y. S. Huh, Novel orange-emitting $Ba_2LaNbO_6:Eu^{3+}$ nanophosphors for NUV-based WLEDs and photocatalytic water purification, *Ceram. Int.*, 2019, **45**, 4781–4789.

56 M. Ghasemi, S. M. Ghoreishian, M. Norouzi, K. Badii, K. Ozaee, C. H. Kwak and Y. S. Huh, Optimization of sonophotocatalytic decolorization of Begazol Black B by loaded, double-sided nanophotocatalysts on porous substrate: A central composite design approach, *J. Taiwan Inst. Chem. Eng.*, 2018, **93**, 166–175.